Discover Mechanical Engineering

RESEARCH Open Access

Brazing of Sn78Cu22 on aluminum substrates observed via in-situ experiments in a large-chamber SEM

Shohreh Khatami[1], Joachim Mayer[1*], Anke Aretz[1], Bei Zhou[2] and Markus Apel[2]

*Correspondence:
Joachim Mayer
mayer@gfe.rwth-aachen.de
[1]Central Facility for Electron Microscopy (GFE), RWTH Aachen University, 52074 Aachen, Germany
[2]Access e. V, Intzestraße 5, 52072 Aachen, Germany

Abstract

In situ brazing is a powerful method for understanding dynamic material behavior during joining process, enabling real-time observation of melting, wetting, and interfacial reactions. The present study investigates the influence of aluminum alloy chemical composition on wetting behavior and interfacial phase formation during soldering with a Sn78Cu22 alloy. The experiments were performed inside a large-chamber scanning electron microscope (LC-SEM) to monitor heat-induced deformation, melting, melt propagation, elemental segregation, and solidification. Microstructural and compositional analyses were carried out using SEM/EDX and TEM, supported by thermodynamic calculations using Thermo-Calc. Despite the low melting point of Sn78Cu22, solder reactions could only be initiated at significantly higher temperatures, namely 466 °C for EN AC-42,100, 500 °C for EN AW-5083, and 600 °C for EN AW-3003, due to the presence of stable surface oxide films. The Si-rich EN AC-42,100 alloy exhibited early filler deformation and formation of Al–Cu and Cu–Sn intermetallic compounds, namely Cu_6Sn_5, Cu_2Sn, while Sn wetting was limited by a Si diffusion barrier. In contrast, the EN AW-5083 and EN AW-3003 alloys showed delayed wetting caused by MgO and $MgAl_2O_4$ oxide layers, respectively. For EN AW-5083, Mg reacted with Sn to form Mg_2Sn within the filler and at the interface, accompanied by Al–Cu formation. For EN AW-3003, Al–Cu interdiffusion led to the formation of Cu-rich Al_4Cu_9-type intermetallics with shallow Sn penetration. These results demonstrate that aluminum alloy chemistry critically governs wetting kinetics and interfacial reactions during soldering with Sn78Cu22.

Keywords LC-SEM, Fluxless brazing, Sn–Cu solder, Aluminum alloys, Intermetallic compounds

1 Introduction

Brazing and soldering of aluminum alloys under vacuum and fluxless conditions are of significant technological interest, particularly for applications where contamination from flux residues must be avoided or where components are sensitive to chemical treatment. However, aluminum joining remains challenging due to the rapid formation of stable oxide layers that hinder wetting and interfacial reactions. Under atmospheric

© The Author(s) 2026. **Open Access** This article is licensed under a Creative Commons Attribution 4.0 International License, which permits use, sharing, adaptation, distribution and reproduction in any medium or format, as long as you give appropriate credit to the original author(s) and the source, provide a link to the Creative Commons licence, and indicate if changes were made. The images or other third party material in this article are included in the article's Creative Commons licence, unless indicated otherwise in a credit line to the material. If material is not included in the article's Creative Commons licence and your intended use is not permitted by statutory regulation or exceeds the permitted use, you will need to obtain permission directly from the copyright holder. To view a copy of this licence, visit http://creativecommons.org/licenses/by/4.0/.

heating, oxide reduction is often ineffective, as oxidation rates increase rapidly with temperature and components may degrade or melt before reaching the critical temperature required for spontaneous oxide decomposition. Consequently, vacuum or protective atmospheres are commonly employed to suppress oxidation, reduce oxygen partial pressure, and enable oxide reduction, as predicted by Ellingham's thermodynamic considerations [1, 2].

Despite extensive studies on aluminum brazing and soldering, most investigations rely on ex-situ characterization, providing only post-processing information on microstructure and phase formation. Direct, real-time insight into wetting, melting, interfacial reactions, and elemental redistribution particularly under fluxless conditions remains limited. This gap is further pronounced for technological aluminum alloys with complex chemical compositions, where alloying elements such as Si, Mg, Cu and Mn strongly influence oxide stability, diffusion behavior, and intermetallic compound formation.

Scanning electron microscopy is a powerful tool widely used in materials science for research, quality control, and failure analysis. However, conventional scanning electron microscopy is typically restricted to small specimens, commonly limited to dimensions of the order of tens of millimeters, which constrains its applicability for realistic joining experiments and in-situ thermal studies [2–5]. In numerous technologically significant applications, traditional scanning electron microscopy is impractical because the specimens requiring investigation cannot be sectioned or modified for SEM analysis. In such cases, the specimen may need to be kept intact for reintegration into a production line, or it could hold historic and/or artistic significance and value. Hence, addressing the challenge of investigating larger sample sizes became imperative. The initial developments in surmounting the challenge of specimen size limitation were made by VisiTec Micro Technik in Germany. In 1994, they introduced the Large Chamber SEM. An innovative instrument featuring a spacious chamber capable of accommodating samples up to 700 mm in diameter and 300 kg in weight. Moreover, it is equipped with a pioneering positioning system that facilitates views from various angles by maneuvering the electron gun and detectors in a controlled manner around the sample. Furthermore, besides its capability for investigating large samples, the LC-SEM holds significant potential for in situ observations of materials under various experimental conditions or even when *operando* mimicking technological processes. Following its introduction, numerous reports detailing the utilization of this device in various research applications have been published [4–9].

In post-mortem investigations, the dynamic behavior of solder alloys during brazing, including critical phenomena such as deformation, elemental segregation, and melting, remains incompletely understood. Furthermore, it is impossible to determine the precise temperatures and conditions at which specific thermodynamic transformations occur. Consequently, key details of the wetting process and interfacial reactions under realistic thermal cycles remain elusive, limiting the ability to optimize joining parameters and to improve joint quality.

The aim of this study is to overcome the limitations of traditional ex-situ characterization techniques, which fail to capture real-time solder behavior during brazing, such as the onset of deformation, segregation, and melting at specific temperatures, by employing in-situ large-chamber scanning electron microscopy (LC-SEM). The target is to directly observe and analyze the dynamic wetting and joining processes of Sn–Cu solder

alloys on aluminum substrates with varying chemical compositions under vacuum and fluxless conditions.

The novelty of our approach lies in the application of the large-chamber scanning electron microscope (LC-SEM), which is equipped with a fast secondary electron (SE) detector, which enables superior spatial and temporal resolution in recording dynamic joining processes. This allows for detailed, real-time observation of each stage of solder phase transformations under the vacuum conditions required for fluxless processing. The study focuses on Sn-Cu alloys, recognized as environmentally friendly, lead-free solders with broad industrial applications. Among various Sn-Cu compositions, Sn78Cu22 is known to exhibit the best wetting behavior, making it particularly suitable for joining aluminum alloys. The comprehensive characterization is further enhanced through a combination of complementary techniques such as energy-dispersive X-ray spectroscopy (EDX), ex situ SEM imaging and transmission electron microscopy (TEM), providing in-depth morphological and chemical insights. Additionally, the experimental findings are correlated with thermodynamic predictions from Thermo-Calc calculations, facilitating a robust understanding of phase evolution and intermetallic compound formation. Together, these capabilities provide unprecedented insight into the influence of aluminum alloy and solder chemistry on wetting kinetics and interfacial reactions during soldering, advancing the knowledge required for optimizing joining processes.

2 Material and method

The experiments utilized the heating module installed within the LC-SEM, which was previously described in an earlier publication [10], albeit with a modification in this study. Instead of employing the top-view configuration, the contact angle mode was adopted to enable a three-dimensional perspective of the joining process. To achieve this, the electron column was positioned at an approximate angle of 85°. Furthermore, the heating module was placed on a laboratory scissor jack to ensure direct alignment with the electron column (Fig. 1). As a precautionary measure for the apparatus, the internal temperature of the chamber was monitored using three strategically positioned thermometers located on both the electron column and the heating module. The chamber pressure was kept constant within the range of $2.9 \pm 0.6 \times 10^{-6}$ mbar.

To investigate the influence of the substrate on the joining process, a series of experiments was carried out using various aluminum alloys as base materials and a Tin-Copper filler alloy (Sn78Cu22). The chemical compositions of the base materials, expressed in weight percent, are listed in Table 1.

For each test, the base sheets were cut into 1×1 cm^2 specimens, mechanically ground and polished, ultrasonically cleaned, and dried. The surface roughness of all base samples was maintained at 60 ± 5 µm. Subsequently, a small filler piece (2×2 mm ± 0.5 mm) was placed on each base material, and the assemblies were then transferred to the heating module inside the LC-SEM. Table 2 summarizes the key experimental parameters used in the in-situ LC-SEM brazing experiments.

2.1 EN-AC 42100 as base

The first test used alloy EN-AC 42100 as the base material. The experimental procedure began with a heating rate of 30 °C/min to reach a final temperature of T = 550 °C (see Supplementary Video S1, the video was recorded during the test). Following the

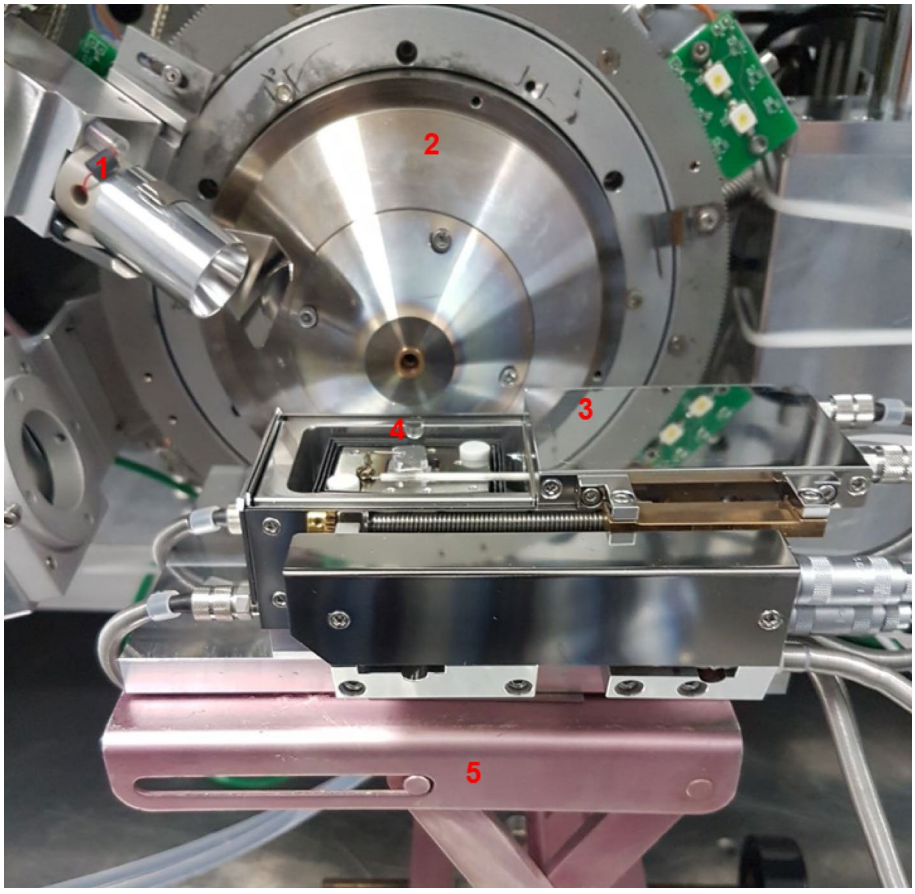


Fig. 1 The heating experiment setup in contact angle mode. (1) SE detector, (2) electron column, (3) heating module, (4) sample, and (5) laboratory scissor jack

Table 1 Chemical composition of utilized base materials in weight-%

Aluminum Alloys	Si	Fe	Cu	Mn	Mg	Cr	Zn	Ti	Other
EN-AW 5083	Max 0.4	Max 0.4	Max 0.1	0.4–1	4–4.9	0.05–0.25	Max0.2	Max0.15	0.05–0.5
EN-AW 3003	Max 0.6	Max 0.7	0.05–0.2	1–1.5	–	–	Max 0.1	–	0.05–0.5
EN-AC 42100	6.50–7.50	0,19	0,05	0,10	0.25–0.45	–	0,07	0.08–0.25	0.05–0.5

completion of the brazing process, the specimens were gradually cooled to room temperature within the vacuum environment of the LC-SEM. The temperature profiles, along with SEM images captured simultaneously during the joining process, are illustrated in Fig. 2.

The corresponding event-log of the experiment is listed in Table 3.

2.2 EN-AW 3003 as base

The subsequent experiment employed alloy EN-AW 3003 as the substrate material. The brazing sequence began with a gradual temperature increase at a rate of 30 °C/min, reaching a stepwise increment up to 600 °C, followed by controlled cooling back to room temperature (see Supplementary Video S2, the video recorded during the test). The temperature profile, accompanied by a series of SEM images, is shown in Fig. 3. The chronological progression of the experiment is documented in the Event-Log shown in Table 4.

Table 2 The key experimental parameters used in the in situ LC-SEM brazing experiments

Parameter	Value/range	Notes
LC-SEM chamber pressure	$(2.9 \pm 0.6) \times 10^{-6}$ mbar	Maintained constant during heating and cooling
Atmosphere	High vacuum (no process gas)	Fluxless brazing conditions
Heating rate	30 °C min^{-1}	Identical for all experiments
Cooling method	Natural cooling under vacuum	No forced cooling
Filler alloy composition	Sn78Cu22 (wt. %)	Lead-free solder
Filler dimensions	(2×2) $mm^2 \pm 0.5$ mm	solid piece
Filler thickness	0.2 mm	
Filler fixing method	Placed directly on substrate (gravity-assisted)	No mechanical fixation or flux
Substrate dimensions	(10×10) mm^2	Thickness identical for all alloys
Surface preparation	Mechanical grinding and polishing	Followed by ultrasonic cleaning
Surface roughness (Ra)	60 ± 5 µm	Measured after preparation
Cleaning procedure	Ultrasonic cleaning in ethanol	Dried in ambient air prior to loading
Observation mode	Contact-angle mode	Electron column tilted ≈ 85°
Imaging detector	Secondary electron (SE) detector	Real-time imaging

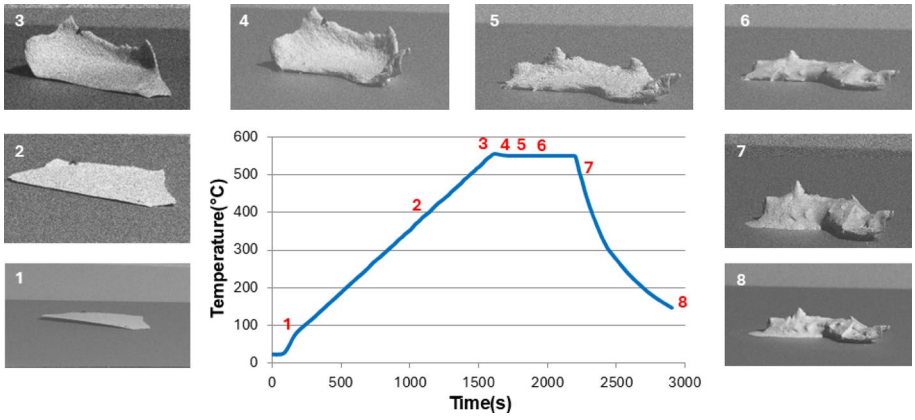


Fig. 2 Thermal curve for brazing process: Sn78Cu22/EN-AC 42100 at max. T = 550 °C

Table 3 Event-log of the experiment: Sn78Cu22/EN-AC 42100 at max. T = 550 °C

Image number	Time (S)	Temperature (°C)	Remarks
1	0	RT	Launch of heat ramp 30 °C /min
2	1340	466	Onset of first deformation of filler in the edges
3	1569	550	Filler deformed upwards
4	1689	550	Filler completely deformed upwards
5	1710	550	Filler shape rounded due to surface tension
6	2162	550	First sign of wetting in edge was observed
7	2355	540	Complete wetting
8	3000	Less than 200	Termination of experiment

2.3 EN-AW 5083 as base

Concluding the series of experiments, EN-AW 5083 segments served as the substrate material for the third test. The brazing procedure commenced with a gradual temperature increase at a rate of 30 °C/min, reaching a stepwise plateau at 600 °C, and concluded with controlled cooling to room temperature (see Supplementary Video S3, the video recorded during the test). The temperature profile, complemented by SEM images, is

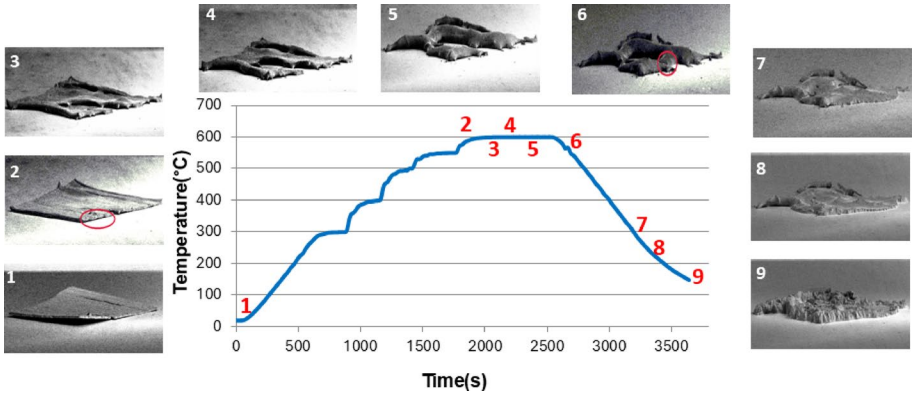


Fig. 3 Thermal curve for brazing process: Sn78Cu22/EN-AW 3003 at max. T = 600 °C

Table 4 Event-log of the experiment: Sn78Cu22/EN-AW 3003 at max. T = 600 °C

Image number	Time (S)	Temperature (°C)	Remarks
1	0	RT	Launch of heat ramp 30 °C /min
2	2041	600	Initial sign of deformation
3	2179	600	Start of segregation phase
4	2225	600	Crack became wider
5	2390	600	The solder reached volume due to the surface tension
6	2695	600	First sign of wetting
7	2707	350	Complete the wetting process of solder
8	2809	300	Solidification phase started
9	3800	Less than 200	Termination of experiment

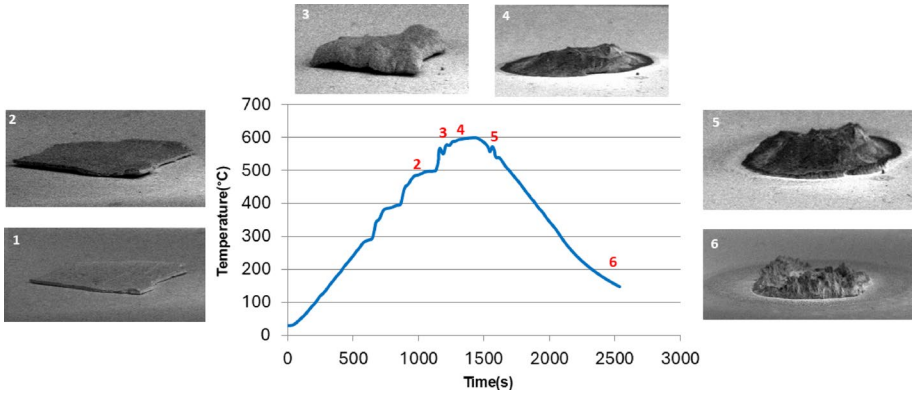


Fig. 4 Thermal curve for brazing process: Sn78Cu22/EN-AW 5083

presented in Fig. 4. Detailed sequential steps of the experiment are documented in the Event-Log, as shown in Table 5.

3 Results and discussion

3.1 Result of brazing of Cu22Sn78/EN-AC 42100

Figure 5a shows optical microscope images of the sample 78Sn22Cu/EN-AC42100, providing a top-view perspective. Notably, discernible alterations in the filler's morphology adjacent to the solder are apparent, meanwhile the heating process yields no impact on the substrate's structural integrity. The height of the solder materials results in 288 µm from its highest point to the substrate surface.

Table 5 Event-log of the experiment: Sn78Cu22/EN-AW 5083 at max. T = 600 °C

Image number	Time (S)	Temperature (°C)	Remarks
1	0	RT	Launch of heat ramp 30 °C /min
2	1162	500	Initial sign of deformation
3	1374	600	The molten solder rises into a dome-like shape due to surface tension, causing it to gain volume
4	1430	600	Initial surface wetting and substrate interaction starts
5	1442	600	Starting the solidification phase, formation of various ring on substrate
6	1503	580- below 200	Termination of experiment

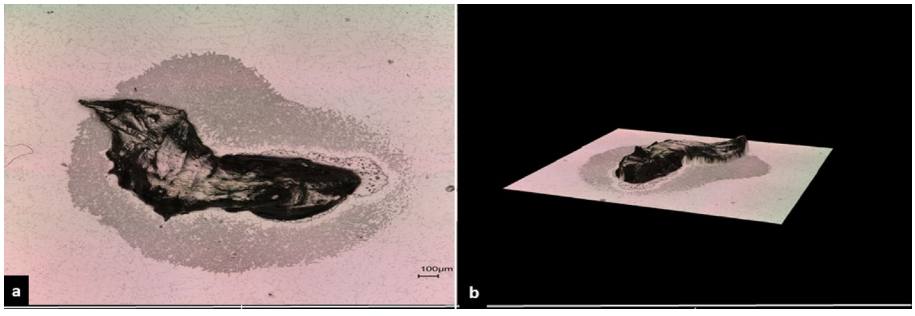


Fig. 5 3D optical microscope images of sample 78Sn22Cu/EN-AC42100. **a** Top view, **b** 3D view

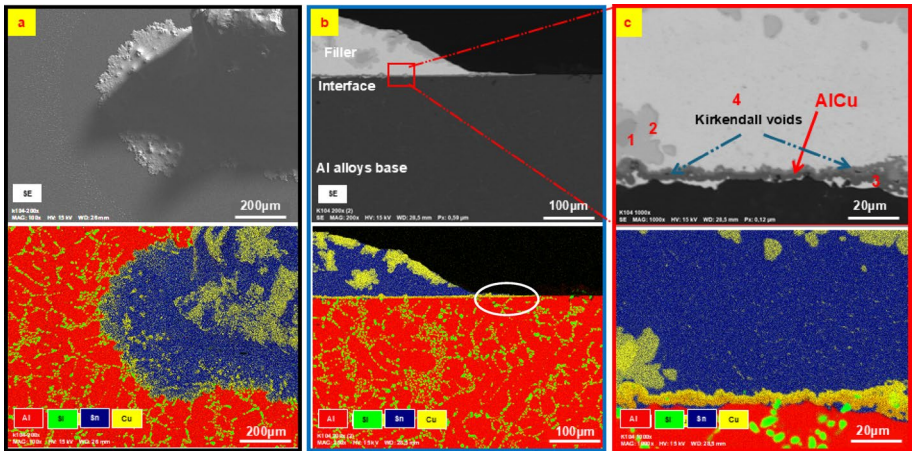


Fig. 6 Top view and cross-section EDX analysis of 78Sn22Cu/EN-AC42100. **a** Top: × 100 top-view SE image of the wetting zone; bottom: top-view EDX maps of Al, Si, Sn, and Cu. **b** Top: × 200 cross-sectional SE image; bottom: cross-sectional EDX maps of Al, Si, Sn, and Cu. **c** Top: × 1000 cross-sectional SE image of the interface border; bottom: EDX maps of Al, Si, Sn, and Cu

The top view and cross-section EDX results are depicted in Fig. 6. Top view EDX analysis were done in the selected wetted area, where the filler overflows on base. The results indicate that Cu and Sn spread on the substrate. Moreover, the changes in the substrate structure around the solder, observed in the microscope images, are associated with the presence of grain boundries accumulation of silicon (Fig. 6a).

The cross-view EDX analysis identifies three distinct regions. Starting with the lowermost segment, corresponding to the substrate, no infiltration of solder constituents is observed. As expected, this zone is predominantly composed of aluminum, with grain boundaries infused with silicon. In the middle region, designated as the boundary

(HAZ), a distinct AlCu layer formation becomes evident. The topmost zone shows the presence of the filler material, where copper remains as the bulk phase, surrounded by tin (Fig. 6b).

The results depict the absence of any penetration of the Cu in the filler into the Al base, meanwhile the interaction is only limited in the HAZ zone. The result of point analysis from the selected 4 points (Fig. 6c) are documented in Table 6. At point 1, the results reveal 22–23 at% Sn, making the two-phase region Cu_3Sn (ε) + $Cu_{41}Sn_{11}$ (δ) stable, which is also in accordance with the phase diagram of Sn-Cu [11]. On the other hand, at point 2, 31–46% Sn is present, making a single-phase Cu_6Sn_5 stable.In the border, where point 3 is indicated, based on the Al-Cu phase diagram[12]; when the atomic percentage of both elements are close to each other (Al-Cu 1:1), the most likely intermetallic in AlCu (η). Zobac et. al. 2019 [12], reported the central part of the diagram and the position of the 1:1 (η) and neighboring phases which is invariant reactions and stable around 500–600 °C. Furthermore, Sn is not able to penetrate to the base which can be due to the fact that 42,100 is a casting alloy with 7% Si, which is stored in the grain boundaries and acts as a diffusion barrier, preventing the filler to infiltrate to the base. Although the grain boundaries offer high-diffusivity paths for atoms due to their disordered lattice, the presence of a second phase (Si), can lead to the drop in the diffusivity. This is due to the fact that Si is close to insoluble in molten Sn, preventing Sn from dissolving into the Si-rich regions (also seen in the Sn-Si phase diagram). Furthermore, the formation of Kirkendall void is evident (Fig. 6c) [13].

The TEM results from the lamella prepared at the interface (area indicated by the white circle in Fig. 6c) are shown in Fig. 7. A large silicon grain is observed at the center of the lamella, separating the pure aluminum from the base material and the tin–aluminum-copper composite phase. Additionally, a small structure located below the silicon grain primarily contains Sn and Mg, as shown in Fig. 7c (based on the42100 data sheet, which includes 0.4% Mg).

3.2 Result of brazing of Cu22Sn78/ En-Aw 3003

Optical microscope images of sample 78Sn22Cu/EN-AW3003 are presented in Fig. 8. In contrast to the previous sample, no discernible new structures or thermal effects are observable in the vicinity of the filler material. The central region of the filler exhibits an approximate height range of 70–150 µm, while this measurement increases to 250 µm at the borders.

Figure 9 represents the SEM top-view and the SEM images of the cross-section and EDX maps. Although wetted regions are not clearly evident, a high concentration of Sn is noticeable on the surface of base, encompassing the soldered area. Conversely, this issue does not apply to copper, as it remains within the solder (Fig. 9a). The cross-section EDX reveals the penetration of Sn into the Al base, which is especially visible in the HAZ zone (Fig. 9b). The 3003 alloy is a wrought Al-Mn alloy with maximum 1% Mn, which

Table 6 The result of EDX point analysis of 78Sn22Cu /EN-AC42100

Point number	Al Atom%	Si Atom%	Cu Atom%	Sn Atom%	Possible phase
1	0.5	0.15	75.61	22.78	$Cu_3Sn + Cu_{41}Sn_{11}$
2	0.85	0.12	57.53	41.50	Cu_6Sn_5 (η/η′)
3	49.65	0.08	48.75	1.52	AlCu (η)
4	0.50	0.01	0.03	99.46	βSn

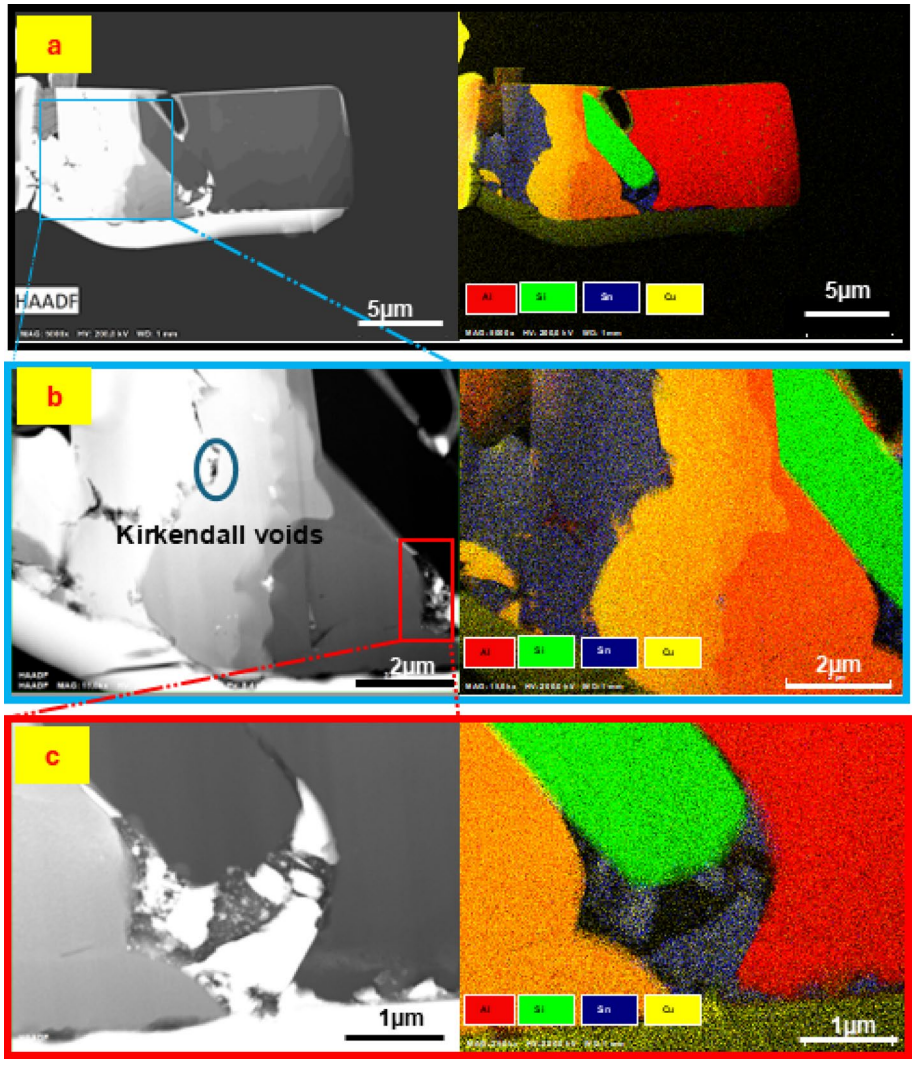


Fig. 7 The TEM HAADF images of **a** x5k lamella, **b** x15k distribution pattern of Si, Al, and, **c** x25k distribution pattern of Sn Cu. Al and Sn are separated by a Si grain. The orange part on the filler side indicates the penetration of aluminum into the filler and the formation of Al–Cu component

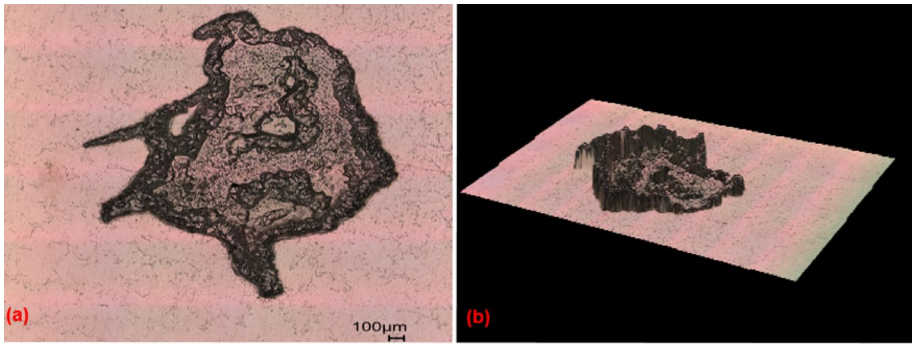


Fig. 8 3D optical microscope images of sample 78Sn22Cu/EN-AW3002. **a** Top view, **b** 3D view

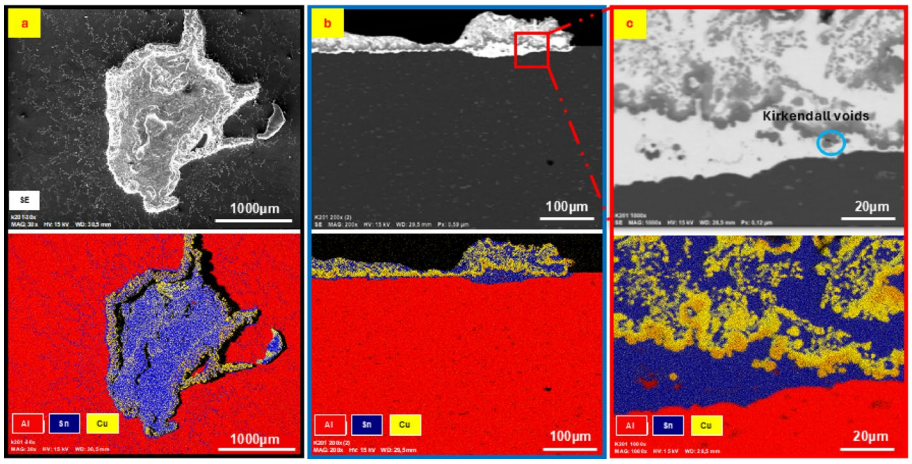


Fig. 9 Top view and cross-section EDX results of 78Sn22Cu/EN-AC42100. **a** Top:×30 top-view SE image of the wetting zone; bottom: top-view EDX maps of Al, Si, Sn, and Cu. **b** Top:×200 cross-sectional SE image; bottom: cross-sectional EDX maps of Al, Si, Sn, and Cu. **c** Top:×1000 cross-sectional SE image of the interface border; bottom: EDX maps of Al, Si, Sn, and Cu

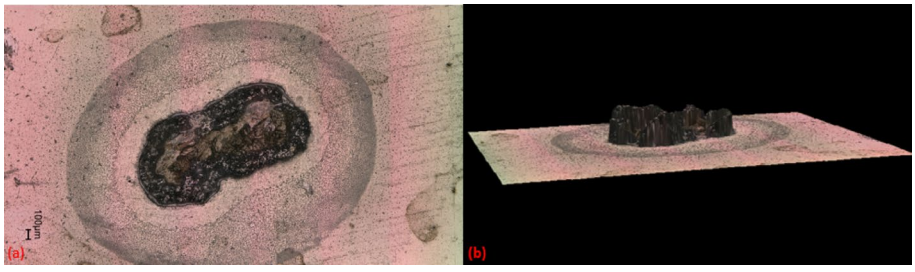


Fig. 10 3D optical microscope images of sample 78Sn22Cu/EN-AW5083. **a** Top view, **b** 3d view

allows the grain boundaries to act as open diffusive paths for molten Sn to penetrate into the Al base, and the Al base to vice versa diffuse into the Sn-Cu filler, leading to better intermixing. Furthermore, since the diffusion rate of Al is much faster than Cu, Al penetrates quicker into the filler (Kirkendall effect) [14], leading to the formation of Al-Cu component. The average point analysis shows the atomic percentage of Cu≈66% and Al≈32%, (in Al-Cu regions) which is in the Cu-rich intermetallic region. The previous studies (Zobac et al., 2019 [12]) showed that the c′, c or d intermetallic phase (Al_4Cu_9-type) occupy roughly the ~ 60–70 at% Cu range at temperatures around 600 °C. However, this phase also remains stable during cooling down to room temperature, and then may only transform to a lower-symmetry distortion (d) or exhibit ordering changes. This includes crystallographic / ordering transitions (c′ ↔ d, possible c′ + d mixtures), including a complete change to a different stoichiometry. Therefore, the presence of the Al_4Cu_9-family at room temperature is expected, possibly in a different structural variant than at 600 °C.

3.3 Result of brazing of Cu22Sn78/ En-Aw 5083

Finally, the experimental results obtained from the Sn78Cu22/EN AW5083 sample are presented. Optical microscope image (Fig. 10) reveals the existence of distinct rings encompassing the solder, each characterized by a unique morphology and structure. Our preliminary hypothesis for this phenomenon focuses on the interplay between substrate

and solder components. Notably, the sample's height, spanning from its highest point to the substrate, ranges from 20 to 60 µm.

The SEM top-view and the images of SEM cross-section EDX maps are shown in Fig. 11. Formation of various rings around the melted solder with significant difference in density and morphology are evident. EDX clearly shows that these rings are made primarily of Mg (from the base) and Sn (from the filler) (Fig. 11a). The first ring surrounding the filler closely, mainly consists of Al, with a small amount of Sn present on top of it. It can be due to the fact that Mg is highly mobile and has a higher vapor pressure relative to the other elements at our working temperature of 600^{O}C. Therefore, the Mg close to the filler evaporates early and spreads towards the near surface region (Fig. 11a). This allows Sn to penetrate to the substrate using the newly formed diffusion paths (due to Mg evaporation), leading to the first ring consisting of Sn alone (Fig. 11a). Further, Sn continues to diffuse to the area with grain boundaries enriched with Mg, wherein the Mg-Sn interaction leads to the formation of the intermetallic component (IMC) Mg_2Sn [15].

In the area with smaller grain size, the effective diffusion rate is higher, which leads to Sn and Mg diffusing faster, resulting in the formation of a wider ring, while the region with bigger grains exhibits a slower diffusion rate, leading to the formation of a matrix ring. These structures express themselves as rings because the molten Sn spreads radially outward from the filler and since the whole process is isotropic, any possible interaction with any other element (here with Mg) leads to the formation of a ring. Cross-section EDX analysis substantiates the penetration of Sn inside the base material, subsequent section diffuse and protrusion at the substrate's surface after traversing a certain distance (Fig. 11b), which is due to the absence of Mg in the grain boundaries and opening of diffusion paths. No sign of diffusion or presence of Cu on the sample surface or at the solder-sample interface is visible. It may be due to the fact that Al exhibits an FCC structure lattice and larger atomic spacing which leads to a higher diffusion rate of Al than Cu, therefore penetrating the filler before Cu is able to move to the base, and forming the IMC AlCu (η) in the filler. The results of point analysis of selected areas in Fig. 11c&a

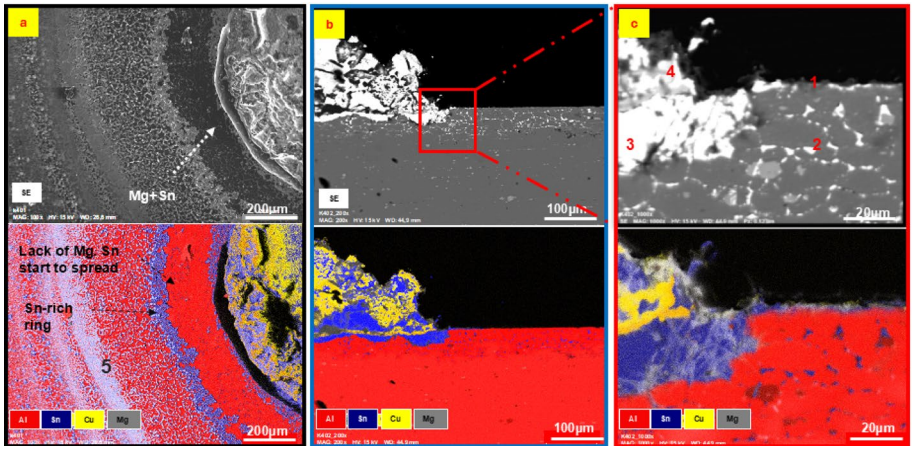


Fig. 11 The SEM images of top and cross-section along with EDX maps of 78Sn22Cu/EN-AC42100 **a** Top:×100 top-view SE image of the wetting zone; bottom: top-view EDX maps of Al, Si, Sn, and Cu. **b** Top:×200 cross-sectional SE image; bottom: cross-sectional EDX maps of Al, Si, Sn, and Cu. **c** Top:×1000 cross-sectional SE image of the interface border; bottom: EDX maps of Al, Si, Sn, and Cu. The presence of Mg on the filler surface vs penetration inside the filler during the brazing is quite evident

Table 7 The result of EDX point analysis of 78Sn22Cu /EN-AW 5083

Point number	Al Atom%	Mg Atom%	Sn Atom%	Cu Atom%	Possible phases
1	80.26	7.11	11.66	1,85	The area before ring formation, where Sn starts to spread on the surface
2	59.09	0	40.76	0	Filling the grain boundaries with Sn due the lack of Mg and opening of diffusion path
3	2.74	0.58	99.05	0,33	Penetration of Sn into base
4	42.71	3.88	0.49	52,71	AlCu (η)
5	8.54	35,52	54.11	1,83	β-Sn (Sn-rich) + Mg_2Sn

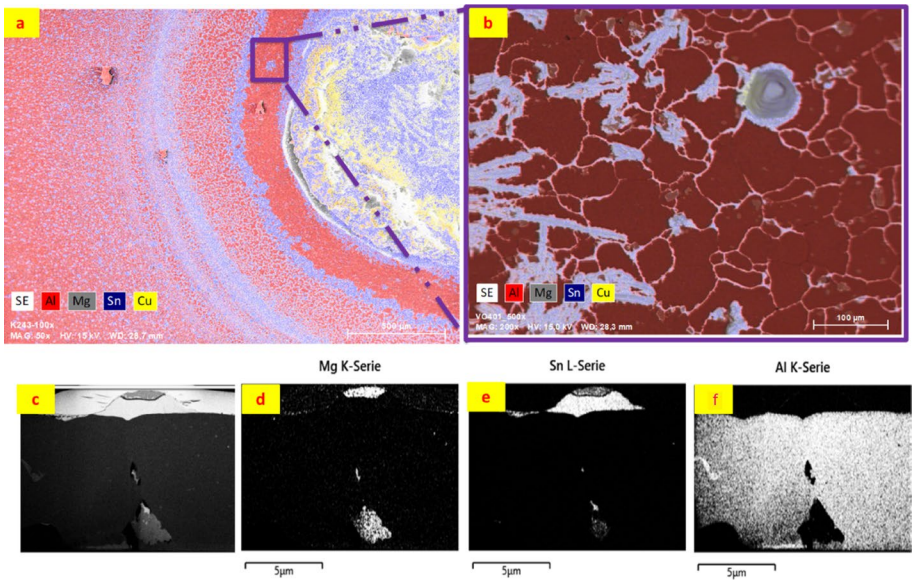


Fig. 12 The top view SEM + EDX maps vs cross-section TEM of sample Sn78Cu22/En-Aw5083. **a** × 100 SE image + EDX of matrix like ring, **b** × 500 SE image + EDX of matrix like ring, **c** x6k HAADF cross view image of lamella, **d** EDX map for Mg, **e** EDX map for Sn, **f** EDX map for Al

are given in Table 7. The lack of Mg is evident at point 1 (region closest to the filler at the surface), due to the evaporation of the filler as aforementioned, meanwhile the simultaneous diffusion of Sn on the surface via the grain boundaries is also visible. Further, the penetration of Sn through the open diffusion paths via the grain boundaries can be seen at point 2. Next, we also see Sn filling in the gaps in the base left behind by Al that previously diffused into the filler at point 3. Lastly, point 4 shows the IMC AlCu in which the diffused Al reacts with Cu, and eventually point 5 is selected data from the area where Mg diffuse to the Sn by migrating toward the grain boundaries and forming the IMC Mg_2Sn. Since we are in Sn-rich region, at a working temperature of 600 °C, we see the presence of two phases including liquid Sn, along with Mg_2Sn. Furthermore, the remaining liquid Sn undergoes the eutectic reaction and solidifies as an $Mg_2Sn + \beta Sn$ (matrix).

The top view EDX plus cross-section TEM images from the matrix ring are illustrated in Fig. 12. The EDX maps indicate a high concentration of metastable Mg_2Sn in the region. Further, some areas show the collective accumulation of Mg (Fig. 12b). The segregation of Mg and Sn in the cross-section TEM image (Fig. 12c) is visible. Mg accumulates at the substrate grain boundaries, while Sn seems to penetrate them. Moreover, the molten Sn overflows on the base and combines with the Mg to form a dome shape wherein the accumulation of Mg at the peak is clearly visible (Fig. 12d and e). It is known

that the density of Sn (7.3 g/cm^3) is higher than Mg (1.7 g/cm^3). Moreover, based on the Mg-Sn phase diagram [15], Mg has very low solubility in liquid Sn, and therefore, instead of dissolving, it segregates. That segregation often localizes at certain surface features which give rise to Mg-rich islands or peaks [16, 17].

Massalski et.al give the melting range of Sn78Cu22 around 227–280 °C based on the binary Sn–Cu phase diagram [18].While our experiments demonstrate that different aluminum substrates show visible reaction of the filler at much higher temperatures: 466 °C on EN AC-42100, 500 °C on EN AW-5083, and 600 °C on EN AW-3003.

Aluminum alloys are naturally covered by a thin but highly stable oxide layer, primarily Al_2O_3, which forms immediately upon exposure to air. Although these films are only a few nanometers thick, they act as an effective barrier to wetting and interfacial reactions with the filler [14]. In the current experiments, which is flux-less under vacuum condition, no chemical agent is available to disrupt or dissolve the oxide film. Consequently, the molten Sn–Cu solder, although thermodynamically melting at 227 °C [19], cannot make contact with the metallic aluminum substrate until the oxide layer is locally broken by thermal stresses, cracking, or diffusion effects. This explains why the solder deformation and wetting starts at temperatures far above the alloy's equilibrium melting point.

In EN AC-42100 (Al–Si casting alloy), the presence of surface Si tends to generate thinner or defective oxide layers, which are easier to disrupt [20]. In EN AW-5083, the high Mg content promotes the formation of MgO and $MgAl_2O_4$, which are thermodynamically more stable than pure alumina and therefore delay wetting [21]. In EN AW-3003, Mn oxides provide a dense and continuous surface film, further increasing the required temperature for the oxide breakdown. Therefore, the observed sequence 42100 < 5083 < 3003 is not governed by the intrinsic melting behavior of the Sn–Cu solder but by the kinetic barrier imposed by alloy-dependent surface oxide films. Without flux, the oxide layer dominates the early stages of soldering in vacuum and shifts the reaction temperature several hundred degrees above the equilibrium melting point.

Thermodynamic equilibrium calculations were carried out using ThermoCalc (version 2025a) with databases TCAL9 and MOBAL8. The material-to-material calculator was employed to model the interaction between the base material and filler material at the investigated temperatures. The calculations enabled the prediction of coexisted equilibrium phases, phase fraction evolution within the reaction zone.

Figure 13 shows the evolution of the AlCu (η) and Cu_3Sn intermetallic phases at 550 °C. The AlCu (η) phase begins to form at ≈0.82–0.90 mass fraction, which is the reaction zone where Al diffuses into the Cu. The present result indicate the act of an Al–Cu intermetallic layer a diffusion barrier. In contrast, Cu_3Sn appear only at very high filler ratios (≈1.0 mass fraction), close to the filler-rich region dominated by Cu-Sn interaction. The absence of Cu_6Sn_5 and $Cu_{41}Sn_{11}$phases in this simulation suggests that at 550 °C these compounds are either unstable or exist in very small quantities below the thermodynamic model's resolution.

Figure 14 presents the phase evolution in the Sn–Cu/3003 system at 600 °C. The diagram illustrates the variation of the volume fraction of each phase during the transition from the aluminium-rich region (left) toward the filler-rich region (right). At low filler fractions (below ≈ 0.2), the FCC_Al phase is dominant, representing the aluminium substrate. As the filler fraction increases, the liquid phase begins to appear (green dashed line in Fig. 14a) and becomes the main constituent between approximately 0.3 and 0.8,

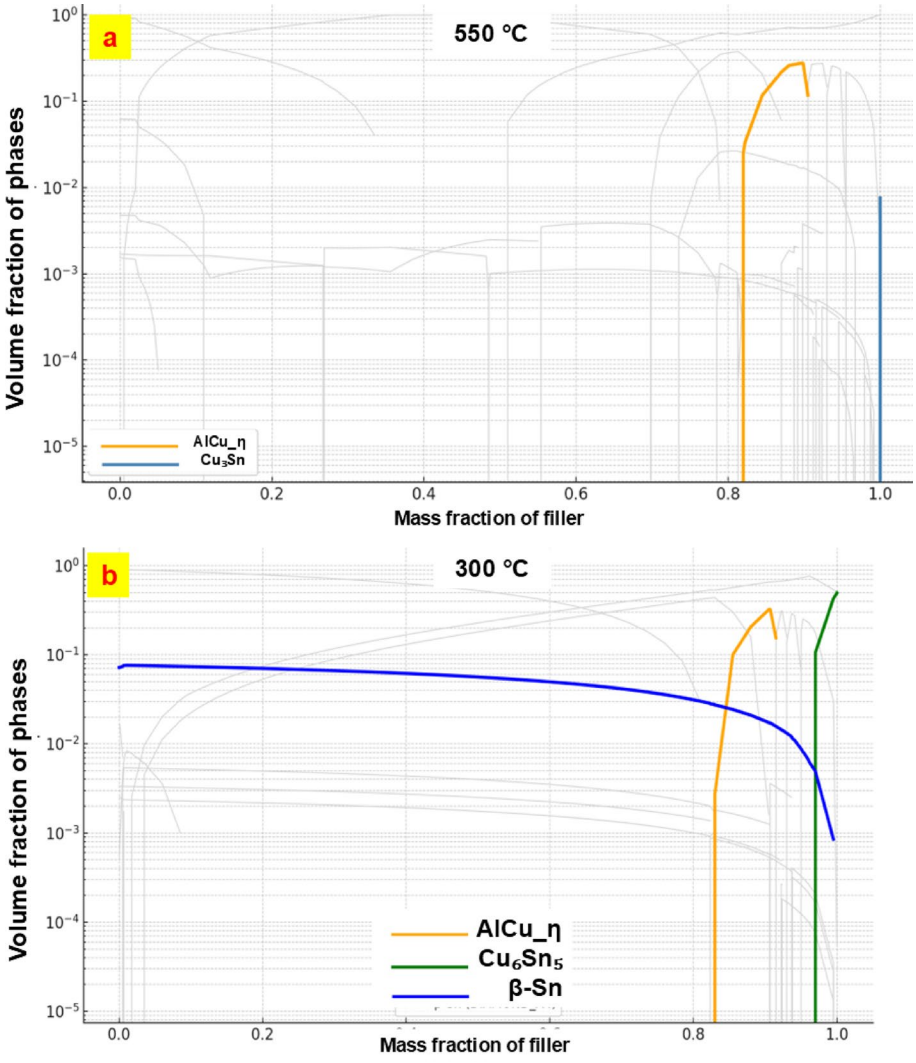


Fig. 13 The phase fraction analysis for sample Sn78Cu22 on En-Ac42100. **a** At 550 °C, and **b** At 300 °C (cooling down)

indicating the melting and mixing behavior of the Sn-Cu filler with the base material. At higher filler contents (above ≈ 0.8), several Cu and Al rich intermetallic compounds emerge. Among them, the AlCu (η) phase shows a significant volume fraction within the range 0.82–0.90, confirming its thermodynamic stability at 600 °C. This phase typically forms at the Al/Cu reaction interface during brazing and is a key intermediate compound that can later transform into $Al_2Cu(\theta)$ upon cooling. Overall, the simulation indicates that at 600 °C the AlCu (η) phase is the most stable Al-Cu intermetallic expected to form near the interface region, while the system remains largely liquid in the central composition range. The disappearance of the liquid phase and the subsequent dominance of solid intermetallic toward the filler-rich side imply a localized solidification and interdiffusion process between molten Sn–Cu and solid aluminium.

Figure 15 demonstrates the calculated phase-fraction for the Sn78Cu22 on EN AW-5083. The evolution of solid and liquid phases clarify the interaction between the aluminium substrate and the Sn-Cu during the brazing process. At 600 °C, the filler is completely molten, and the phase constitution is dominated by a Sn-rich liquid. Under

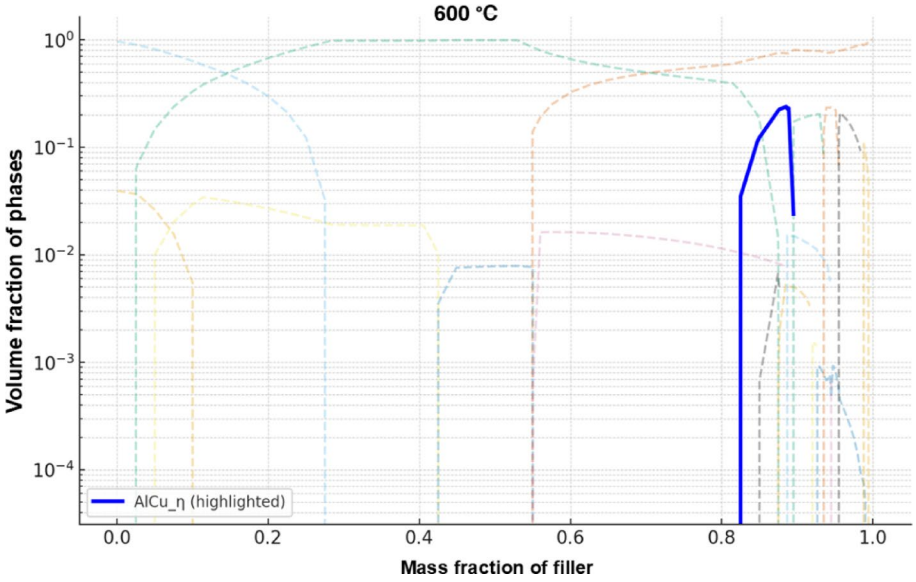


Fig. 14 The phase fraction analysis for the sample Sn78Cu22 on En-Aw3003

these conditions, diffusion of Al into molten filler leads to the formation of the AlCu (η) intermetallic phase. This phase represents the primary reaction product and provides a metallurgical connection between the two materials. The calculation shows Mg containing compounds are stable at this stage, as Mg remains either in solid solution within the aluminium substrate or dissolved in the Sn-rich melt. When the temperature decreases, the proportion of liquid Sn declines and the β-Sn phase begins to solidify. Meanwhile, AlCu(η) continues to grow, maintaining strong metallurgical bonding. The coexistence of solid β-Sn and AlCu(η) at this temperature promotes interfacial integrity by combining the Sn matrix with a rigid Al-Cu intermetallic network. Upon further cooling, the solid fraction of β-Sn increases significantly, and the overall phase equilibrium shifts toward solid-state conditions. While AlCu(η) remains stable at the interface, an additional phase, Mg_2Sn, is expected to form as a consequence of Mg super saturation in the solidifying Sn matrix. Although Mg_2Sn is not explicitly predicted in the equilibrium datasets, its formation is thermodynamically favoured once the Sn-rich liquid transforms into β-Sn, leading to local Mg enrichment and subsequent reaction with Sn. Based on the Mg-Sn binary phase diagram, the onset of Mg_2Sn formation occurs near 500 °C, with notable precipitation between ≈450 °C and 300 °C, corresponding to the rapid reduction of Mg solubility in Sn. Consequently, Mg_2Sn typically appears along Sn-rich regions or at the Al/Sn interface as discrete particles or ring-shaped segregations, in agreement with experimental observations in Mg-containing aluminium alloys. Below 300 °C, Mg_2Sn remains stable and coarsens during cooling.

4 Conclusions

The main goal of the current study was to understand the influence of substrate composition on the brazing behavior of Sn78Cu22 on three different Al alloys (EN AC-42100, EN AW-5083, and EN AW-3003). The in situ brazing inside the large-chamber SEM in fluxless and vacuum conditions gave us a chance for real-time observation of the filler and surface substrate changes as well as each phase transformation (segregation, melting, wetting, and solidification) occurring in the system.

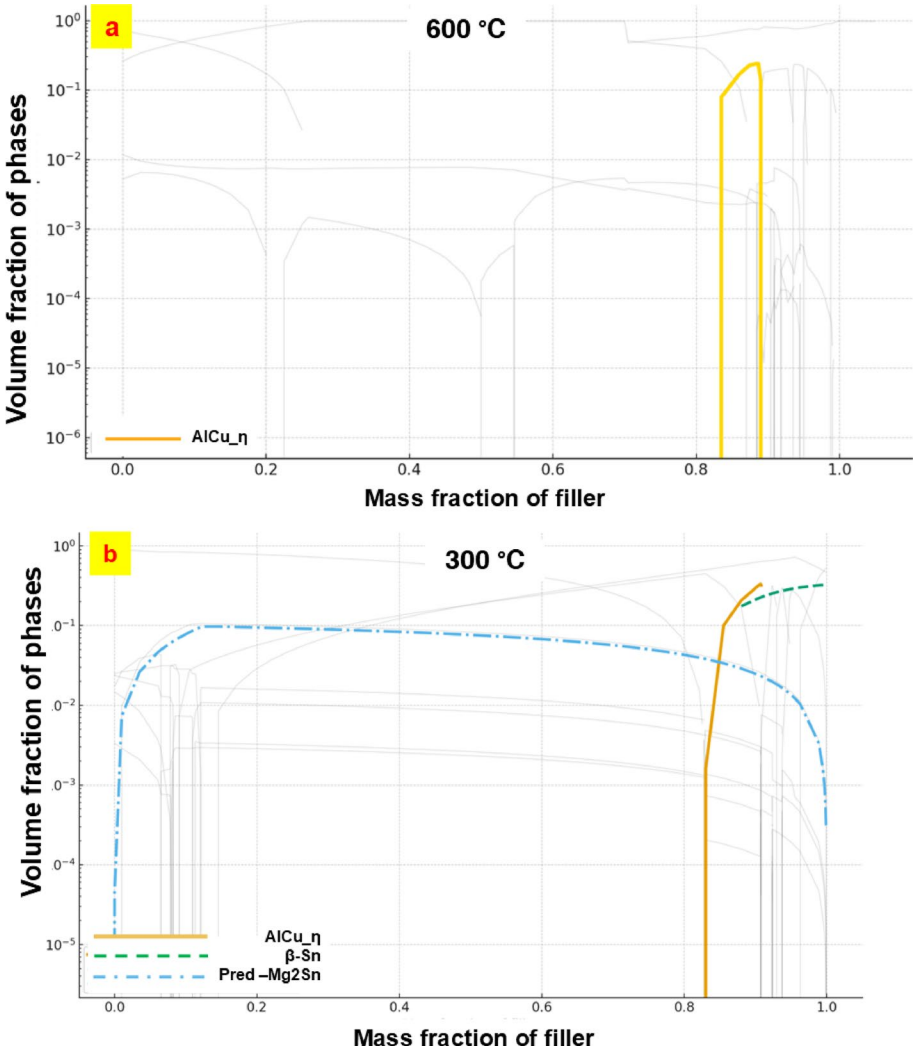


Fig. 15 The phase fraction analysis for Sn78Cu22 on En-Aw5083. **a** At 550 °C, and **b** At 300 °C (cooling down)

Despite the low melting point of Sn78Cu22, solder reaction and melting processes started at much higher temperatures (466 °C for EN AC-42100, 500 °C for EN AW-5083, and 600 °C for EN AW-3003), which can be due to the presence of surface oxide films.

The Si-rich 42,100 alloy showed earlier filler deformation and formation of AlCu and Cu–Sn intermetallic (Cu_6Sn_5, Cu_3Sn) at the interface, with minimal Sn wetting due to the Si diffusion barrier. In contrast, 5083 and 3003 showed delayed wetting, due to the stable $MgO/MgAl_2O_4$ stable oxide films, respectively. For 5083, Mg tended to interact with Sn to form Mg_2Sn (inside the filler and as a ring on the base surface), while AlCu formed near the interface as Al diffused into the filler. For 3003, mutual diffusion between Al and Cu in the molten filler was evident, leading to Cu-rich Al_4Cu_9-type intermetallic formation, while Sn penetration remained shallow.

Overall, the brazing behavior of Sn–Cu filler on aluminum is generally controlled by the presence of the oxide layer as well as the material composition of the base, emphasizing the value of *in-situ* LC-SEM for studying real-time joining mechanisms. The summarized conclusion is written in Table 8.

Table 8 Summary of brazing behavior of Sn78Cu22 on different aluminum alloys under fluxless vacuum conditions

Substrate alloy	Onset temperature of solder reaction/ melting (°C)	Dominant surface oxide/ diffusion barrier	Wetting behavior	Main interfacial reactions and phases formed	Key observations
EN AC 42100	~466	Si-rich surface layer acting as diffusion barrier	Early filler deformation; limited Sn wetting	Formation of AlCu and Cu–Sn intermetallics (Cu_6Sn_5, Cu_3Sn) at the interface	Si inhibits Sn wetting but promotes early intermetallic formation
EN AW 5083	~500	Stable MgO / $MgAl_2O_4$ oxide layer	Delayed wetting	Mg_2Sn formation inside the filler and as a surface ring; AlCu formation near the interface	Strong Mg–Sn interaction; oxide layer delays wetting
EN AW 3003	~600	Stable Al oxide layer	Strongly delayed wetting	Mutual Al–Cu diffusion; Cu-rich Al_4Cu_9-type intermetallics; shallow Sn penetration	High reaction temperature; limited Sn interaction with substrate
General trend	Alloy-dependent, higher than Sn–Cu melting point	Oxide layer controlled by substrate chemistry	Fluxless wetting strongly delayed	Intermetallic formation governed by substrate elements (Si, Mg, Cu)	Brazing behavior controlled by oxide stability and alloy composition

Supplementary Information

The online version contains supplementary material available at https://doi.org/10.1007/s44245-026-00209-8.

Supplementary Material 1

Supplementary Material 2

Supplementary Material 3

Supplementary Material 4

Acknowledgements
This work was supported by the Deutsche Forschungsgemeinschaft (DFG) in the framework of the Collaborative Research Centre SFB1120, project A06. We also thank Shriya Agarwal for her valuable feedback which greatly improved this work.

Author contributions
S.K. designed and performed the in-situ experiments, analysed SEM/EDX/TEM data, and wrote the main manuscript text.A.A. assisted with LC-SEM setup, in-situ heating configurations, and data acquisition.J.M. supervised the project, provided scientific guidance, and contributed to manuscript revision.B.Z. conducted Thermo-Calc simulations and contributed to interpretation of thermodynamic results.M.A. supported modelling work, reviewed the simulation results, and contributed to the discussion section.All authors reviewed and approved the final manuscript.

Funding
Open Access funding enabled and organized by Projekt DEAL. This work was funded by the Deutsche Forschungsgemeinschaft (DFG) within the framework of the Collaborative Research Centre SFB 1120, project A06.

Data availability
The data supporting the findings of this study are available from the corresponding author upon reasonable request.

Declarations

Ethics approval and consent to participate
Not applicable. This study did not involve human participants or animals.

Consent for publication
Not applicable.

Competing interests
The authors declare no competing interests.

Received: 24 November 2025 / Accepted: 2 March 2026
Published online: 12 March 2026

References

1. Hawksworth DK. Advances in brazing: 19. Chapters: Fluxless brazing of aluminium. Elsevier Inc.; 2013.
2. Sekulic DP. Brazing of aluminum alloys. Aluminum Science and Technology. ASM International; 2018. pp. 763–82. https://doi.org/10.31399/asm.hb.v02a.a0006529
3. Sugiyama Y. Brazing of aluminium alloys. Weld Int. 1989;3(8):700–10.
4. Schulz B, Sandmann D, Gilbricht S. SEM-based automated mineralogy and its application in geo-and material sciences. Minerals. 2020;10(11):1004. https://doi.org/10.3390/min10111004.
5. FRAHM E. Scanning electron microscopy (SEM): Applications in archaeology. Encyclopedia of global archaeology, 2014, S. 6487–6495. https://doi.org/10.1007/978-1-4419-0465-2_341
6. Romero A. Overcoming challenges in material science testing with the use of large specimen SEM analysis. Microsc Today. 2007;15(5):32–5. https://doi.org/10.1017/S1551929500061216.
7. Tillmann W, Pfeiffer J, Sievers N, Boettcher K. Analyses of the spreading kinetics of AgCuTi melts on silicon carbide below 900 C, using a large-chamber SEM. Colloids Surf A Physicochem Eng Aspects. 2015;468:167–73. https://doi.org/10.1016/j.colsurfa.2014.12.039.
8. Mayer J, Kallinna J, Watermeyer P, Aretz A, Rehbach W, Linke J, et al. Non-destructive analysis of engineering components in the large-chamber scanning electron microscope. Microsc Microanal. 2007;13(S02):1010–1. https://doi.org/10.1017/S1431927607074314.
9. Fried M, Krechel C, Affeldt EE, Eckert B, Kimmig S, Retze U, Göken M. Fatigue crack initiation in nickel-based superalloys studied by microstructure-based FE modeling and scanning electron microscopy. In: MATEC Web of Conferences (Vol. 14, p. 16001). EDP Sciences. 2014, https://doi.org/10.1051/matecconf/20141416001.
10. Aretz A, Ehle L, Haeusler A, Bobzin K, Öte M, Wiesner S, et al. In situ investigation of production processes in a large chamber scanning electron microscope. Ultramicroscopy. 2018;193:151–8. https://doi.org/10.1016/j.ultramic.2018.07.002.
11. Leineweber A. The Cu–Sn system: a comprehensive review of the crystal structures of its stable and metastable phases. J Phase Equilibria Diffus. 2023;44(3):343–93. https://doi.org/10.1007/s11669-023-01041-3.
12. Zobac O, Kroupa A, Zemanova A, Richter KW. Experimental description of the Al-Cu binary phase diagram. Metall Mater Trans A. 2019;50(8):3805–15. https://doi.org/10.1007/s11661-019-05286-x.
13. Wang J, Chen J, Zhang L, Zhang Z, Han Y, Hu X, et al. Forming mechanism and growth of Kirkendall voids of Sn/Cu joints for electronic packaging: a recent review. J Adv Join Process. 2022;6:100125. https://doi.org/10.1016/j.jajp.2022.100125.
14. Laurila T, Vuorinen V, Kivilahti JK. Interfacial reactions between lead-free solders and common base materials. Mater Sci Eng R Rep. 2005;49(1–2):1–60. https://doi.org/10.1016/j.mser.2005.03.001.
15. Ghosh P, Mezbahul-Islam MD, Medraj M. Critical assessment and thermodynamic modeling of Mg–Zn, Mg–Sn, Sn–Zn and Mg–Sn–Zn systems. Calphad. 2012;36:28–43. https://doi.org/10.1016/j.calphad.2011.10.007.
16. Xu L, Liu X, Sun K, Fu R, Wang G. Corrosion behavior in magnesium-based alloys for biomedical applications. Materials. 2022;15(7):2613. https://doi.org/10.3390/ma15072613.
17. Zhuo X, Zhao L, Gao W, Wu Y, Liu H, Zhang P, et al. Recent progress of Mg–Sn based alloys: the relationship between aging response and mechanical performance. J Mater Res Technol. 2022;21:186–211. https://doi.org/10.1016/j.jmrt.2022.08.126.
18. Okamoto H, Schlesinger ME, Mueller EM (Eds) Alloy phase diagrams. ASM international. 2016. https://doi.org/10.31399/asm.hb.v03.9781627081634.
19. Zhao M, Zhang L, Liu ZQ, Xiong MY, Sun L. Structure and properties of Sn-Cu lead-free solders in electronics packaging. Sci Technol Adv Mater. 2019;20(1):421444. https://doi.org/10.1080/14686996.2019.1591168.
20. Yin LM, Xian JW, Yao ZX. Comparison of wettability for Sn-based solders on copper and aluminum substrates. In: Materials Science Forum (Vol. 687, pp. 15–20). Trans Tech Publications Ltd. 2011; https://doi.org/10.4028/www.scientific.net/MSF.687.15
21. Hosking M, Yost FG. The mechanics of solder alloy wetting and spreading. Berlin: Springer; 2012.

Publisher's note

Springer Nature remains neutral with regard to jurisdictional claims in published maps and institutional affiliations.